

# NMWC - isentropic model (WS 2020/21)

## Experiments on downslope windstorms

**Author**

Michael Binder

c-Number: 11843166

### 1 Introduction

This report continues on the work of developing a two-dimensional isentropic model to study the nonlinear flow of a stratified atmosphere past a mountain ridge. In general, the model is capable of simulating moist flow with simple cloud microphysics parameterizations like the warm-rain bulk-microphysics scheme following Kessler (Kessler, 1969), but this report is mainly focused on the investigation of a phenomenon called downslope windstorm. Nevertheless, the effect of moist processes coupled with the dynamics are considered as well.

After introducing the isentropic model in the next section, theories on downslope windstorms will be presented in section 3 before multiple experiments and results are discussed in section 4.

### 2 The 2D isentropic model

Isentropic models significantly simplify the simulation and investigation of an idealized adiabatic flow. Since the vertical coordinate is expressed in potential temperature  $\theta$ , the vertical wind velocity vanishes, because potential temperature is conserved for adiabatic flow regimes (Equation 1).

$$\dot{\theta} = \frac{d\theta}{dt} = 0 \quad (1)$$

The result is a stack of  $\theta$ -layers that can be represented by a set of equations formally identical to the shallow water equations by using an advective model formulation. The main equations are the horizontal momentum equation (Equation 2) with the Montgomery potential  $M$ , the continuity equation (Equation 3) with the isentropic density  $\sigma = -\frac{1}{g} \frac{\partial p}{\partial \theta}$ , and the hydrostatic relation (Equation 4).

$$\frac{Du}{dt} = -\left(\frac{\partial M}{\partial x}\right)_\theta \quad (2)$$

$$\frac{\partial \sigma}{\partial t} + \left(\frac{\partial \sigma u}{\partial x}\right)_\theta = 0 \quad (3)$$

$$\Pi = \frac{\partial M}{\partial \theta} \quad \text{with} \quad \Pi = c_p \left(\frac{p}{p_{ref}}\right)^{\frac{R}{c_p}} \quad (4)$$

The equations are discretized by finite differences in space and time on a staggered grid, neglecting earth's rotation ( $f = 0$ ) and with a constant isentropic surface as the lower boundary condition ( $\theta_s = \text{const}$ ). Moist diabatic processes can be included through parameterizations and coupled to the dynamics to account for vertical advection, too.

### 3 Theory on downslope windstorms

The basis of downslope windstorms in idealized models refers to a relation between the altitude of an existing shear layer in the atmosphere above the mountain and the properties of the prevailing background flow. The background flow, or more precisely the wind speed  $u$  and stability  $N$  (Brunt-Vaisalla frequency) of the atmosphere, define the vertical wavelength of hydrostatic waves that develop for flows over a mountain ridge (Equation 5).

$$\lambda_z = \frac{2\pi U}{N} \quad (5)$$

While Peltier and Clark (solving time-dependent linear wave equation) defined the critical altitude for the shear layer that could lead to downslope windstorms with respect to this vertical wavelength as  $\frac{1}{4}\lambda_z + \frac{n}{2}$  with  $n=0,1,\dots$  (Peltier and Clark, 1979), Smith had a different approach (solving Long's equation) and ended up describing the whole range between  $n \cdot \frac{1}{4}\lambda_z$  and  $n \cdot \frac{3}{4}\lambda_z$  as favorable for downslope windstorms (Smith, 1985).

Though their approaches differed in terms of the underlying equations, their basic physical assumptions were consistent. Both assumed a wave-induced, turbulent critical layer, which is well-mixed and has a constant potential temperature. This layer acts as a boundary and reflects upward propagating waves back towards the mountain. If the altitude of the critical layer and the wavelength of the vertically propagating waves match considering the stated relations, the reflections produce a resonant wave, trap the wave energy below the well-mixed layer and lead to increasing wind speeds close to the surface on the lee side of the mountain (Durran and Klemp, 1987).

In the following section it is tried to identify parameters and settings of the isentropic model that can reproduce or influence this nonlinear phenomenon. In general, linear theory of mountain waves begins to break down when the perturbation velocity ( $u'$ ) becomes large compared with the basic flow  $U$ . This happens when the mountain height  $h_m$  becomes very high,  $U$  very slow, or the stability  $N$  very high. The non-dimensional mountain height  $\epsilon$  (equation 6) is a measure of this nonlinearity and might indicate the occurrence of nonlinear phenomena like wave breaking, flow blocking or downslope windstorms.

$$\epsilon = \frac{h_m N}{U} \quad (6)$$

Miles and Huppert defined a critical  $\epsilon$  of 0.85 for continuously stratified and hydrostatic flow over a 2D bell-shaped mountain. Larger values are expected to produce wave breaking and/or flow blocking (Miles and Huppert, 1969). Though wave breaking can not be represented in the isentropic model, effects of the critical mountain height on the development of downslope windstorms can very well be investigated and will be considered in section 4.

It has also been shown that different mountain shapes can lead to different critical values for  $\epsilon$  (Miles and Huppert, 1968 or Huppert and Miles, 1969). While most investigations are conducted with the Gaussian bell shaped mountain (equation 7), it will also be compared to the Witch of Agnesi mountain (equation 8).

$$h_{Gauss}(x) = h_m \cdot e^{-\left(\frac{x}{a}\right)^2} \quad (7)$$

$$h_{Agnesi}(x) = h_m \cdot \frac{a^2}{x^2 + a^2} \quad (8)$$

With  $a$  being the half width at half maximum of the mountains the Gaussian bell shaped mountain has a steeper slope angle compared to the Witch of Agnesi mountain. They are more or less similar in the peak region, but the Witch of Agnesi is flatter at lower elevations and can be distinguished from 0 throughout the whole domain, while the Gaussian shape is basically 0 towards the boundaries.

## 4 Experiments and results

Table 1 lists relevant parameters for all important model runs, which are discussed in the following subsections. Based on the first experiment the horizontal domain and resolution was adjusted adequately to resolve downslope windstorms with the isentropic model. The half width  $a$  of the mountain ridge is 20km for all simulations and the potential temperature at the surface is  $\theta_0 = 280K$ . If not stated otherwise, all plots refer to a simulation time of 12h with a mountain growth time of 2h to avoid CFL violations at startup.  $\Delta t$  is set to 2s to avoid CFL violations overall together with a horizontal diffusion coefficient of 0.3. Moist processes are only considered when mentioned and neglect ice- or mixed-phase processes (Kessler scheme).

The range of the colorbar for the horizontal velocity plots was intentionally set from 0 to  $40 \frac{m}{s}$  for an intuitive interpretation and comparison of all plots. Additionally, some figures have been moved to the appendix A to ensure a fluent reading.

### 4.1 Resolution matters

As previously mentioned, horizontal resolution is an important factor that has to be considered when representing downslope windstorms with a numerical model. Multiple settings, which were supposed to produce a downslope windstorm, failed at first due to a coarse resolution. Figure 1 visualizes this significant difference in the flow regime by only varying the number of horizontal grid points. While the model with a  $\Delta x$  of 2500m peaks at wind speeds of  $22 \frac{m}{s}$ , similar runs with a higher resolution of  $\Delta x = 1000$  result in wind speeds above  $32 \frac{m}{s}$  (Figure 1 (b)).

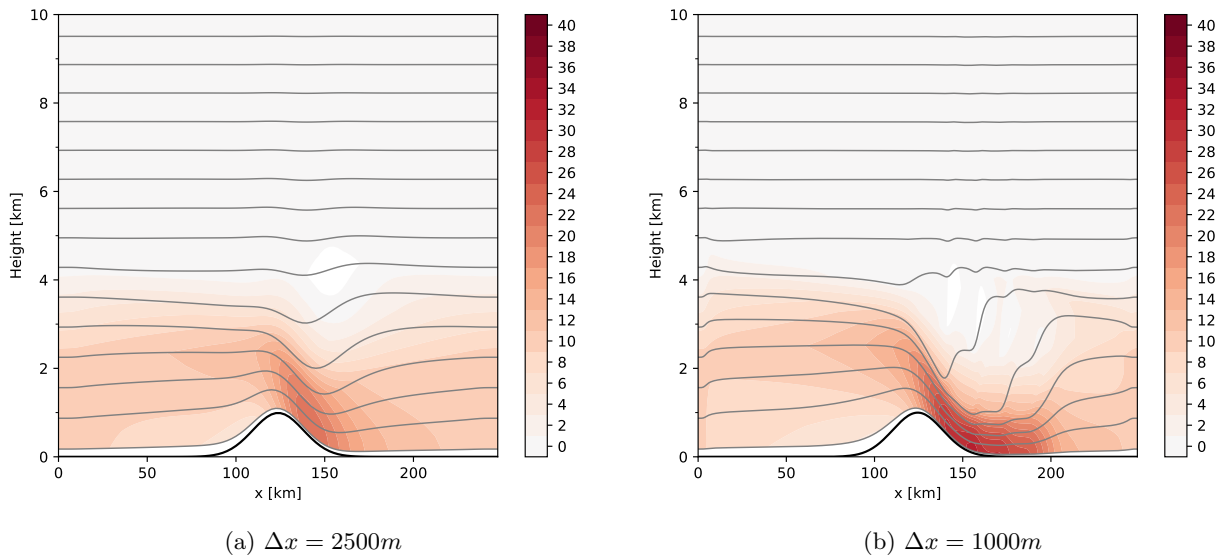


Figure 1: Comparison of model outputs for varying horizontal resolution. A downslope windstorm with diverging isentrops over the mountain only develops for resolutions of  $\Delta x$  around 1km and smaller.

In order to avoid very long simulation runs for further investigations, the horizontal domain is reduced to 150km to lower the number of horizontal grid points, while keeping the resolution at  $\Delta x = 1km$ . This proved to be a good compromise without disturbing the flow across the mountain by model boundaries significantly.

### 4.2 Shear layer altitude and $\lambda_z$

The first variation of the model parameters proves the dependency of downslope windstorms on the shear layer altitude as described in section 3. Moving the shear layer up to an altitude between 5.5km and 7.1km ( $k=16-21$ ) leads to a rather hydrostatic wave regime with upstream tilted phase lines as shown in figure 2 (a) and not to a downslope windstorm. This fits the theory of Peltier, Clark and Smith, because the shear layer is now located at an altitude of  $\approx \lambda_z$ . In addition, placing the shear

Table 1: Summary of most important model run settings to ensure reproducibility.  $k_{sl}$  refers to the position of the shear layer, it is marked red, when the shear layer does not match the stated requirement for a critical layer in section 3. Simulation runs marked purple consider moist processes.

u (m/s)	N (1/s)	$\lambda_z$ (km) (Shear layer)	$h_m$ (m)	a (km)	$\epsilon$ (-) (Mtn shape)	$\Delta x$ (m)	W-storm ( $u_{max}$ )
10	0.01	6.28 ( $k_{sl} = 6 - 12$ )	1000	20	1 (Gaussian)	2500	No (22)
10	0.01	6.28 ( $k_{sl} = 6 - 12$ )	1000	20	1 (Gaussian)	1000	Yes (32)
10	0.01	6.28 ( $k_{sl} = 16 - 21$ )	1000	20	1 (Gaussian)	1000	No (30)
10	0.01	6.28 ( $k_{sl} = 25 - 30$ )	1000	20	1 (Gaussian)	1000	Yes (32)
10	0.01	6.28 ( $k_{sl} = 6 - 12$ )	500/600	20	0.5/0.6 (Gaussian)	1000	No (21)
10	0.01	6.28 ( $k_{sl} = 6 - 12$ )	700/800	20	0.7/0.8 (Gaussian)	1000	Yes (26)
10	0.01	6.28 ( $k_{sl} = 6 - 12$ )	600	20	0.6 (Agnesi)	1000	No (18)
10	0.01	6.28 ( $k_{sl} = 6 - 12$ )	700	20	0.7 (Agnesi)	1000	Yes (22)
10	0.01	6.28 ( $k_{sl} = 6 - 12$ )	600	20	0.6 (Lee hill)	1000	No (21)
10	0.01	6.28 ( $k_{sl} = 6 - 12$ )	700	20	0.7 (Lee hill)	1000	Yes (26)
10	0.01	6.28 ( $k_{sl} = 6 - 12$ )	1000	20	1 (Gaussian)	1000	Yes (32)
10	0.01	6.28 ( $k_{sl} = 6 - 12$ )	1000	20	1 (Lee hill)	1000	Yes (32)
15	0.01	9.42 ( $k_{sl} = 6 - 12$ )	500	20	0.33 (Gaussian)	1000	No (28)
15	0.01	9.42 ( $k_{sl} = 6 - 12$ )	700	20	0.46 (Gaussian)	1000	Yes (35)
15	0.01	9.42 ( $k_{sl} = 11 - 17$ )	800	20	0.53 (Gaussian)	1000	No (28)
15	0.01	9.42 ( $k_{sl} = 11 - 17$ )	900	20	0.6 (Gaussian)	1000	Yes (37)

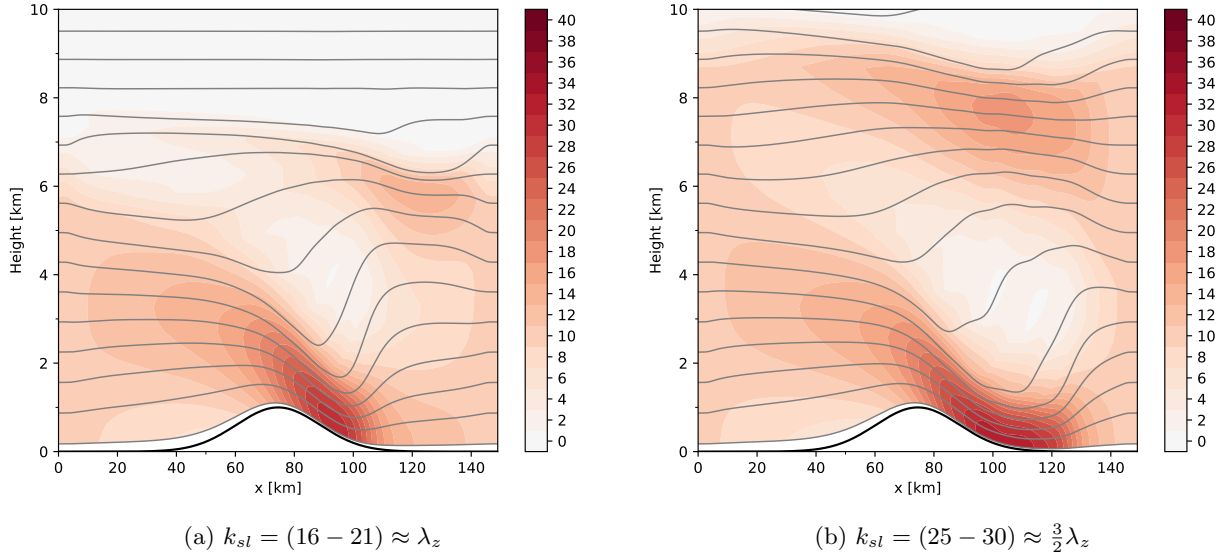


Figure 2: Comparison of model outputs for varying the shear layer altitude considering the vertical wavelength of hydrostatic waves induced by the background conditions. Simulation runs were extended to 24h to ensure stationary results.

layer even higher at  $\approx \frac{3}{2}\lambda_z$  ( $k_{sl}=25-30$  or 8.4-9.9km) results again in a flow regime that suggests a more or less mixed region above the lee slope with strongly compressed isentropes below (figure 2 (b)). The pattern is not as pronounced as in the lower shear layer case from figure 1 (b), but wind speeds again exceed  $32 \frac{m}{s}$  and are higher compared to a shear layer outside the critical region.

### 4.3 The non-dimensional mountain height $\epsilon$

As described in section 3,  $\epsilon$  is a measure to identify nonlinear patterns in a 2D stratified flow past an obstacle like a mountain ridge. A downslope windstorm is one of these patterns, which can actually be represented in an isentropic model unlike breaking waves with overturning isentropes. Figure 1 (b) shows a downslope windstorm for  $\epsilon = 1$  and, consequently, raises the question how far  $\epsilon$  needs to be reduced to avoid a downslope windstorm for this specific mountain shape. Figure ?? visualizes four model runs with varying mountain height representing  $\epsilon$  values between 0.5 and 0.8. Though  $\epsilon = 0.7$  can still be considered a downslope windstorm due to its prominent bend in the isentropes above the mountain top, it is already close to some kind of transition phase. The flow for  $\epsilon = 0.6$  on the other side should be assigned to a hydrostatic wave regime, because the isentropes are still following the wave pattern with an upstream tilted phase line, instead of collapsing towards the surface on the mountain's lee side.

Wind speeds increase for higher mountains throughout all simulation runs, but show a more significant change between  $\epsilon = 0.6$  and  $\epsilon = 0.7$ , which further supports a change in the flow regime. Changing the Brunt-Vaisalla frequency  $N$  has an almost similar effect on  $\epsilon$  as changing the mountain height  $h_m$ , but it has to be considered that the stability ( $N$ ) contributes to the vertical wavelength of the hydrostatic waves, too. The shear layer has to be adjusted.

### 4.4 Variations of the mountain shape

As expected, wind speeds were lower for the Witch of Agnesi mountain shape due to its overall lower slope angle. Nevertheless, a change in the flow regime occurred at approximately the same non-dimensional mountain height as the for the Gaussian mountain shape (Figure 5). The change is less pronounced, but the shape of the isentropes are of sufficient evidence and fit to the relatively stronger increase in wind speed between  $\epsilon = 0.6$  and  $\epsilon = 0.7$ .

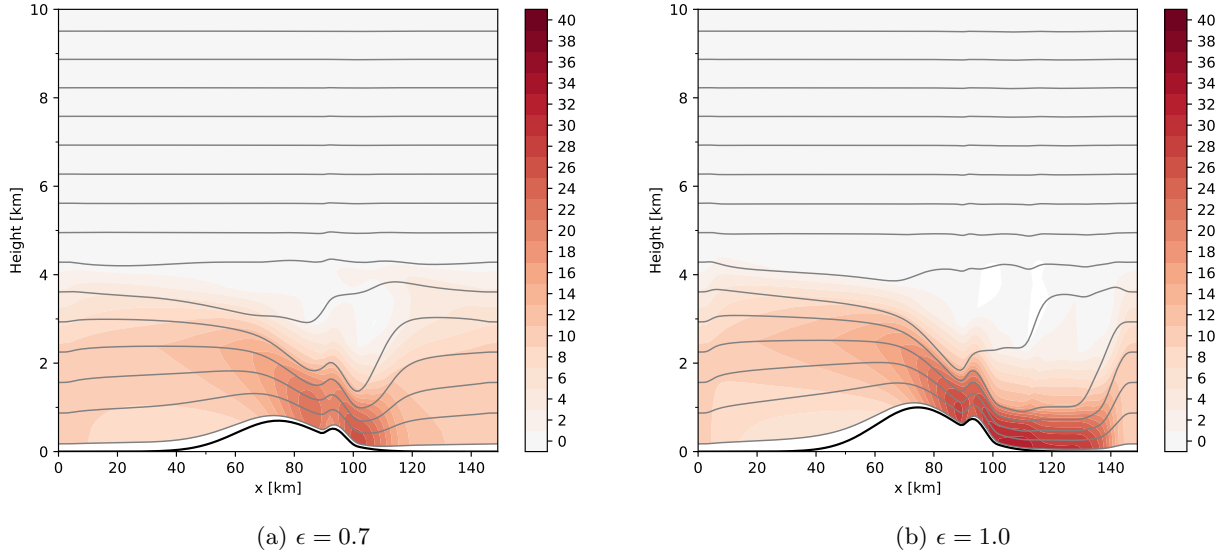


Figure 3: Visualization of model outputs for two non-dimensional mountain heights  $\epsilon$  with a small hill on top of the main mountain's lee slope. A downslope windstorm develops in both scenarios just like in the symmetric mountain shape case.

In another variation that includes a modification of the topography the influence of a non-symmetrical mountain shape is investigated. A smaller hill with similar, but smaller shape is placed on top of the lee side slope of the original mountain. It is basically a shifted mountain that is only considered for grid points where its topography is higher than the topography of the main mountain. As a result, the shape of the original mountain is not changed and variations in the flow can only be related to the additional elevation. The corresponding source code can be found in appendix B. Since the isentropic model is not able to represent any turbulence or flow separation at the surface due to the quite strong change in terrain gradients, the flow and isentropes follow the shape of the hill in the lee of the mountain. It turns out that the adjustment of lee slope barely influences the flow regime. Besides the terrain following shape of the isentropes, downslope windstorms or hydrostatic mountain waves do not change significantly. Even the maximum wind speed of a certain scenario does not change compared to simulation runs with the original mountain topography (compare table 1 and figure 3). The only thing that might be mentioned is the smoother descent of the isentropes over the peak of the main mountain for a downslope windstorm regime. This is also visualized in figure 3, which shows the model output for two non-dimensional mountain heights that lead to a downslope windstorm.

#### 4.5 Moisture and precipitation effects

So far, the simulated atmosphere has been assumed to be dry. In this section, the model is adapted to include moist processes using the warm-rain bulk-microphysics scheme (Kessler, 1969) with a coupling of diabatic forcings (like condensational heating) to the dynamics of the model. Moisture is introduced by setting six model layers close to saturation starting with the third layer (code is not provided since trivial).

Though vertical velocities  $\dot{\theta}$  are introduced through these moist processes, no noticeable effects on the downslope windstorm regime are observed. Even the maximum wind speed of  $u_{max} = 32 \frac{m}{s}$  is consistent with dry model runs (compare second run in table 1 with the moist (purple) simulations further down).

More interesting is the observation of more accumulated rain after 12h simulation time on the windward side of the ridge, when including a small hill on the lee side. Most precipitation still occurs slightly upstream of the mountain peak, but with the lee hill it rains significantly more even further upstream (Figure 4). When analyzing individual time steps of the simulations, it becomes clear that this additional precipitation occurs at the very beginning of the simulation just after finishing the mountain

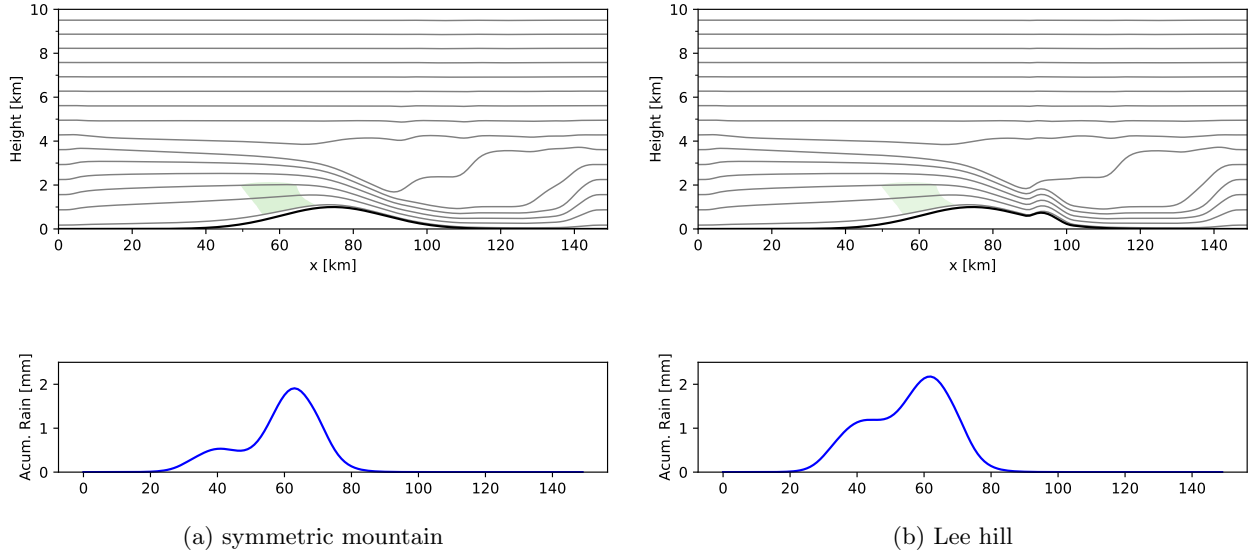


Figure 4: Comparison of accumulated rain after 12h simulation time for two downlope windstorm regimes. The first simulation has a symmetric mountain shape, the second simulation has a small hill on top of the main mountain's lee slope. Moist processes are parameterized with the Kessler scheme and coupled to the dynamics.

growth (slow increase of mountain topography to actual size). Thus, this observation is most likely a model artifact due to non-stationary processes at the beginning of the simulation.

## 4.6 Wind speed $u$

In a last experiment the background wind speed below the shear layer has been increased to  $15 \frac{m}{s}$ . At first, the altitude of the shear layer is kept at the same altitude as before, because it just fits the lower boundary of the critical range at  $\frac{1}{4}\lambda_z$  as described in section 3. For a second set of model runs the shear layer has been adjusted to match the center of the critical range again at  $\frac{1}{2}\lambda_z \approx 4.7km$ . Related parameters and settings are listed in table 1.

As long as the shear layer is at the same altitude as before ( $\approx 2.5 - 4km$ ) the key difference to a wind speed of  $10 \frac{m}{s}$  is the non-dimensional mountain height at which the flow regime changes to a downslope windstorm. Instead of  $\epsilon$  the actual mountain height  $h_m$ , at which the flow regime changed, stayed more or less the same resulting in a notable difference for  $\epsilon$ . Figure 6 visualizes the transition between  $h_m = 500m$  ( $\epsilon = 0.33$ ) and  $h_m = 700m$  ( $\epsilon = 0.46$ ). It was hard to assign a regime to the transitional height  $h_m = 600m$ , so it was left out. The maximum wind speed also increased from  $28 \frac{m}{s}$  ( $h_m = 500m$ ) to  $35 \frac{m}{s}$  ( $h_m = 700m$ ).

For a shear layer between  $\approx 3.8 - 5.7km$  this observation changed. As visualized in the lower two plots of figure 6, the transition to a downslope windstorm appeared for a higher mountain height of  $900m$  ( $\epsilon = 0.6$ ). The stronger increase in wind speed from  $u_{max} = 28 \frac{m}{s}$  ( $h_m = 800m$ ) to  $u_{max} = 37 \frac{m}{s}$  ( $h_m = 900m$ ) indicates the transition, too.  $\epsilon$  is still a bit lower compared to the standard case with  $u = 10 \frac{m}{s}$ , but it is in the same range unlike  $\epsilon = 0.46$  for the transition height with a lower shear layer. It makes clear how important the altitude of the shear layer is with respect to the vertical wavelength of the hydrostatic waves that develop over the mountain ridge. Even an adaption within the critical range influences the flow regime underneath.

## 5 Conclusion

It is already clear that the downslope windstorm regime is quite sensible to a wide range of flow and model parameters. As always, model resolution has to be high enough to actually resolve the phenomenon of interest and corresponding model settings (for example domain or time step) have to be adjusted adequately to avoid complications during the simulation (for example violation of the

CFL criterion).

Though important nonlinear phenomena for downslope windstorms like wave breaking (overturning isentropes) over the mountain's lee slope are not represented in an isentropic model, it is still possible to achieve a comparable flow regime following linear theory (compare with Smith, 1985) with a more or less mixed layer above the lee slope representing the breaking region. Nevertheless, this limit of the isentropic model makes it hard to define critical thresholds for parameters like the non-dimensional mountain height  $\epsilon$  to distinguish between a hydrostatic wave regime and a downslope windstorm. The change of the regime is rather represented by a transitional phase of key parameters than by an abrupt change, but an idealized and conceptual analysis is still valid.

As an extension to this work, a variation of the Brunt-Vaisalla frequency could be investigated as mentioned in section 4.3. This implies a vertical adjustment of the shear layer, which led to interesting results in section 4.2. It might be interesting to compare different gradients in the shear layer or analyse different altitudes with respect to  $\lambda_z$  in more detail than in this paper.

## References

- Durrán, D. R., & Klemp, J. B. (1987). Another look at downslope winds. part ii: Nonlinear amplification beneath wave-overturning layers. *Journal of Atmospheric Sciences*, *44*(22), 3402–3412. [https://doi.org/10.1175/1520-0469\(1987\)044<3402:ALADWP>2.0.CO;2](https://doi.org/10.1175/1520-0469(1987)044<3402:ALADWP>2.0.CO;2)
- Huppert, H. E., & Miles, J. W. (1969). Lee waves in a stratified flow part 3. semi-elliptical obstacle. *Journal of Fluid Mechanics*, *35*(3), 481–496. <https://doi.org/10.1017/S0022112069001236>
- Kessler, E. (1969). On the distribution and continuity of water substance in atmospheric circulations. *On the distribution and continuity of water substance in atmospheric circulations* (pp. 1–84). American Meteorological Society. [https://doi.org/10.1007/978-1-935704-36-2\\_1](https://doi.org/10.1007/978-1-935704-36-2_1)
- Miles, J. W., & Huppert, H. E. (1968). Lee waves in a stratified flow. part 2. semi-circular obstacle: Appendix. *Journal of Fluid Mechanics*, *33*(4), 803–814. <https://doi.org/10.1017/S0022112068001680>
- Miles, J. W., & Huppert, H. E. (1969). Lee waves in a stratified flow. Part 4. Perturbation approximations. *Journal of Fluid Mechanics*, *35*(3), 497–525. <https://doi.org/10.1017/S0022112069001248>
- Peltier, W. R., & Clark, T. L. (1979). The evolution and stability of finite-amplitude mountain waves. part ii: Surface wave drag and severe downslope windstorms. *Journal of Atmospheric Sciences*, *36*(8), 1498–1529. [https://doi.org/10.1175/1520-0469\(1979\)036<1498:TEASOF>2.0.CO;2](https://doi.org/10.1175/1520-0469(1979)036<1498:TEASOF>2.0.CO;2)
- Smith, R. B. (1985). On severe downslope winds. *Journal of Atmospheric Sciences*, *42*(23), 2597–2603. [https://doi.org/10.1175/1520-0469\(1985\)042<2597:OSDW>2.0.CO;2](https://doi.org/10.1175/1520-0469(1985)042<2597:OSDW>2.0.CO;2)



## A Additional figures supporting the discussion

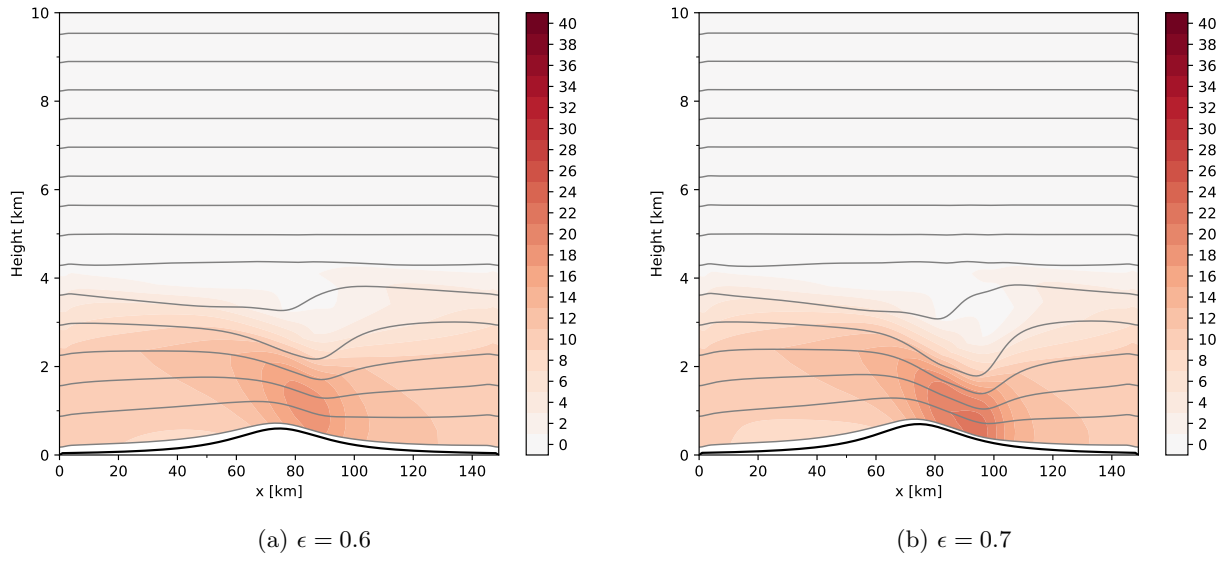
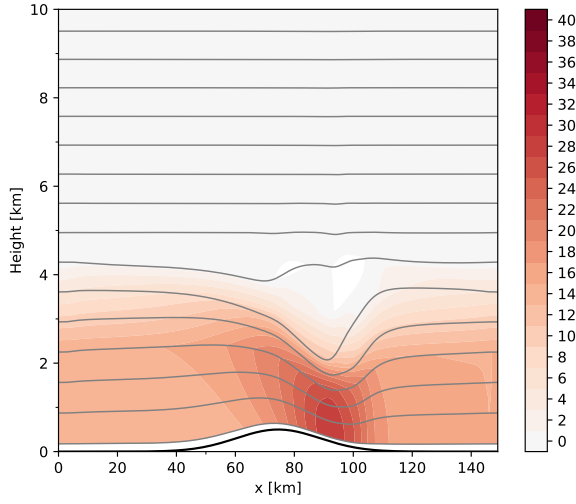
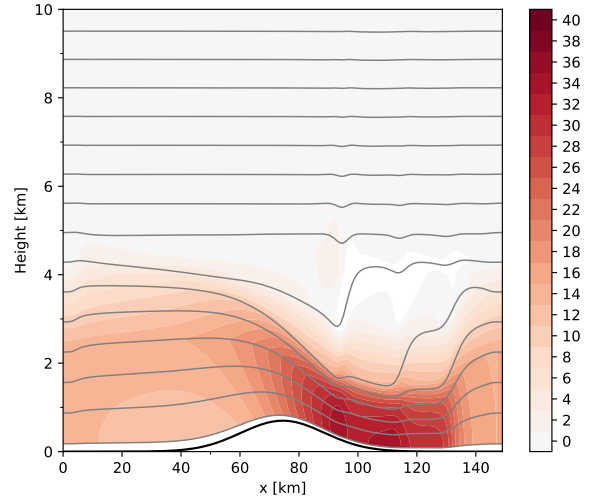


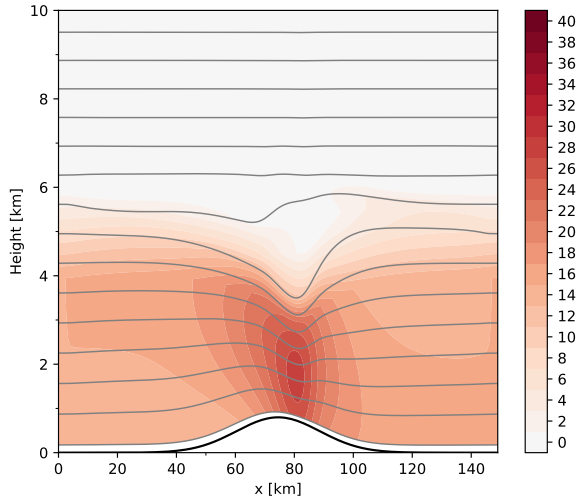
Figure 5: Comparison of model outputs for a varying non-dimensional mountain height  $\epsilon$  for the Witch of Agnesi mountain. Again a downslope windstorm starts to develop for  $\epsilon = 0.7$ .



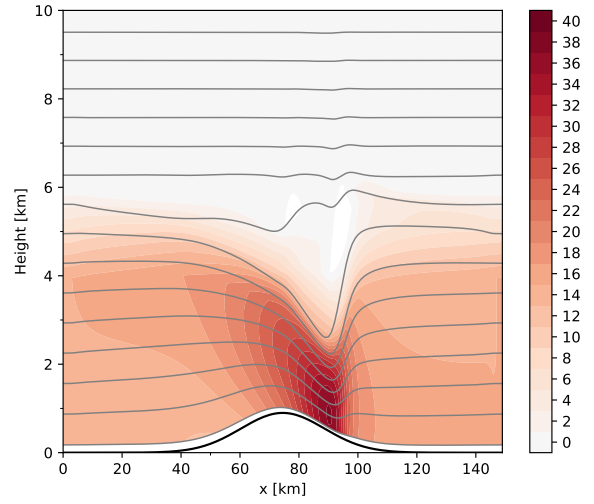
(a)  $\epsilon = 0.33$  with  $k_{sl} = 6 - 12$



(b)  $\epsilon = 0.46$  with  $k_{sl} = 6 - 12$



(c)  $\epsilon = 0.53$  with  $k_{sl} = 11 - 17$



(d)  $\epsilon = 0.6$  with  $k_{sl} = 11 - 17$

Figure 6: Visualization of model outputs for two shear layer altitudes and two non-dimensional mountain heights  $\epsilon$  respectively with a background wind speed of  $u = 15 \frac{m}{s}$ . A downslope windstorm develops for  $\epsilon = 0.46$  (lower shear layer) and  $\epsilon = 0.6$  (upper shear layer).

## B Source code adjustment for mountain topography

```

7  def maketopo(topo,nxb):
8      """
9      Topography definition
10
11      Input: maketopo(topo,nxb)
12      Output: topo
13      """
14      if idbg == 1:
15          print('Topography ...\\n')
16
17      x = np.arange(0,nxb,dtype='float32')
18
19
20      if mtn_topo==1: # lee mtn
21          x0 = (nxb - 1)/2. + 1
22          x1 = (nxb - 1)*leeHill_rel + 1
23          x_lee = (x+1 - x1)*dx
24          x = (x+1 - x0)*dx
25
26          topomf_main = topomx*np.exp(-(x/float(topowd))**2)
27          topomf_lee = topomx*h_ratio*np.exp(-(x_lee/float(topowd*w_ratio))**2)
28          topomf = np.where(topomf_main>topomf_lee,topomf_main,topomf_lee)
29
30      elif mtn_topo==2: # downstream mtn
31          x0 = (nxb - 1)/2. + 1
32          x1 = (nxb - 1)*2*(leeHill_rel+5/32) + 1
33          x_lee = (x+1 - x1)*dx
34          x = (x+1 - x0)*dx
35
36          topomf_main = topomx*np.exp(-(x/float(topowd))**2)
37          topomf_lee = topomx*h_ratio*np.exp(-(x_lee/float(topowd*w_ratio))**2)
38          topomf = np.where(topomf_main>topomf_lee,topomf_main,topomf_lee)
39
40      elif mtn_topo==3: # Witch of Agnesi mtn
41          x0 = (nxb - 1)/2. + 1
42          x = (x+1 - x0)*dx
43
44          topomf = topomx * topowd**2 / (x**2 + float(topowd)**2)
45
46      elif mtn_topo==4: # Witch of Agnesi mtn with lee hill
47          x0 = (nxb - 1)/2. + 1
48          x1 = (nxb - 1)*leeHill_rel + 1
49          x_lee = (x+1 - x1)*dx
50          x = (x+1 - x0)*dx
51
52          topomf_main = topomx * topowd**2 / (x**2 + float(topowd)**2)
53          topomf_lee = topomx*h_ratio * float(topowd*w_ratio)**2 / (x_lee**2 + float(topowd*w_ratio)**2)
54          topomf = np.where(topomf_main>topomf_lee,topomf_main,topomf_lee)
55
56      else:
57          x0 = (nxb - 1)/2. + 1
58          x = (x+1 - x0)*dx
59          topomf = topomx*np.exp(-(x/float(topowd))**2)
60
61      topo[1:-1,0] = topomf[1:-1] + 0.25*(topomf[0:-2] - 2.*topomf[1:-1] +
62          topomf[2:])
63
64
65      return topo

```

Figure 7: Source code adjustment for mountain topography variations.